Science Advances
AAAS

Supplementary Materials for

A handheld intelligent single-molecule binary bioelectronic system for fast and reliable immunometric point-of-care testing

Eleonora Macchia *et al.*

Corrresponding author. Fabrizio Torricelli, fabrizio.torricelli@unibs.it; Luisa Torsi, luisa.torsi@uniba.it

Sci. Adv. **8**, eabo0881 (2022)
DOI: 10.1126/sciadv.abo0881

The PDF file includes:

Other Supplementary Material for this manuscript includes the following:

Supplementary Text

Section S1. Video of a typical assay

A video showing the whole assay procedure comprising all the needed steps is provided. The video clearly show how easy is to perform the assay as very few steps are needed and the manual operations are very minimal requiring no sample treatment at all. It also shows how fast the whole assay is.

Section S2. Thickness uniformity and stability of physisorbed antibodies on a gold surface

The uniformity and the long-term stability of the SARS-CoV-2 Spike-S1 antibodies, (anti-S1) layer physisorbed on a gold surface, is assessed *via* Surface Plasmon Resonance (SPR) characterization. To this aim, a Multi-Parameter SPR (MP-SPR) Navi 200-L apparatus in the Kretschmann configuration was used(*46*) and a schematic of the apparatus is shown in **Figure S1a**. An optical glass coated with a gold (~ 50 nm) on chromium (~2 nm) layer, serves as a semi-transparent SPR slide (BioNavis Ltd). The slide is allocated in the sample-holder placed into the SPR flow-through cell in which the solution for the bio-layer deposition or the phosphate buffer solution for the subsequent washing step (to remove the few proteins that were not stably physisorbed on the gold surface), is injected. The thickness of the deposit is inspected *via* the evanescent wave generated by a laser beam (λ = 670 nm) totally reflecting on the Au-covered optical glass.(*47*, *48*) The gold exposed area, about 0.4 cm^2, was inspected simultaneously in two different points (3 mm apart) to assess the thickness uniformity of the deposited layer.

The SPR slide was then put in contact with a solution of anti-S1 and the antibodies physisorption on the slide was monitored *in-situ* and real-time. This was carried out by static injection in the SPR cell of 100 µL of the anti-S1 capturing antibodies (100 µg/mL) phosphate buffer solution (PBS, ionic strength i_s 163 mM and pH 7.4). The optical signal changes occurring as the biolayer was deposited, were recorded as a function of time. All the experiments were performed at 24°C. The measured SPR transient traces, measured in two different points, are given as red and blue curves in **Figure S1b**. The almost identical traces evidence the high thickness homogeneity of the anti-S1 surface coverage.

The PBS anti-S1 solution was kept in contact with the gold surface for 1.5 hours. The rapid increase of the optical signal (**Figure S1b**), indicates that a physisorbed film of anti-S1 immediately forms on the slide, reaching 95% of the coverage in 15 minutes. The deposited film was rinsed with PBS and a negligible 2% loss of antibodies is observed in the timeframe of a typical bioelectronics sensing experiment (20 minutes).

The surface coverage of anti-S1 physisorbed on the gold surface was quantitatively assessed, as costumery in SPR experiments, by means the de Feijter's equation (**Equation S1**):(*49*)

$$\Gamma = d \cdot (n - n_0) \cdot \left(\frac{dn}{dC}\right)^{-1} \qquad \text{(S1)}$$

where Γ, expressed in ng·cm^{-2}, is the surface coverage, d the thickness of the biolayer deposited on the gold surface, n-n_0 is the difference between the refractive index of the adlayer and that of

the bulk medium while *dn/dC* is the specific refractivity of the adsorbed biolayer. Deriving this further to account for the instrument response, it returns **Equation S2**:

$$(n - n_0) = \Delta\theta_{SPR} \cdot k \qquad \text{(S2)}$$

where k is the wavelength dependent sensitivity coefficient, and $\Delta\theta_{SPR}$ is the experimental angular shift. For a $\lambda = 670$ nm laser beam a thin layer ($d < 100$ nm), the following approximations hold true: $dn/dC \approx 0.182$ cm^3 g^{-1} and $k \cdot d \approx 1.0 \cdot 10^{-7}$ cm deg.(*50*)

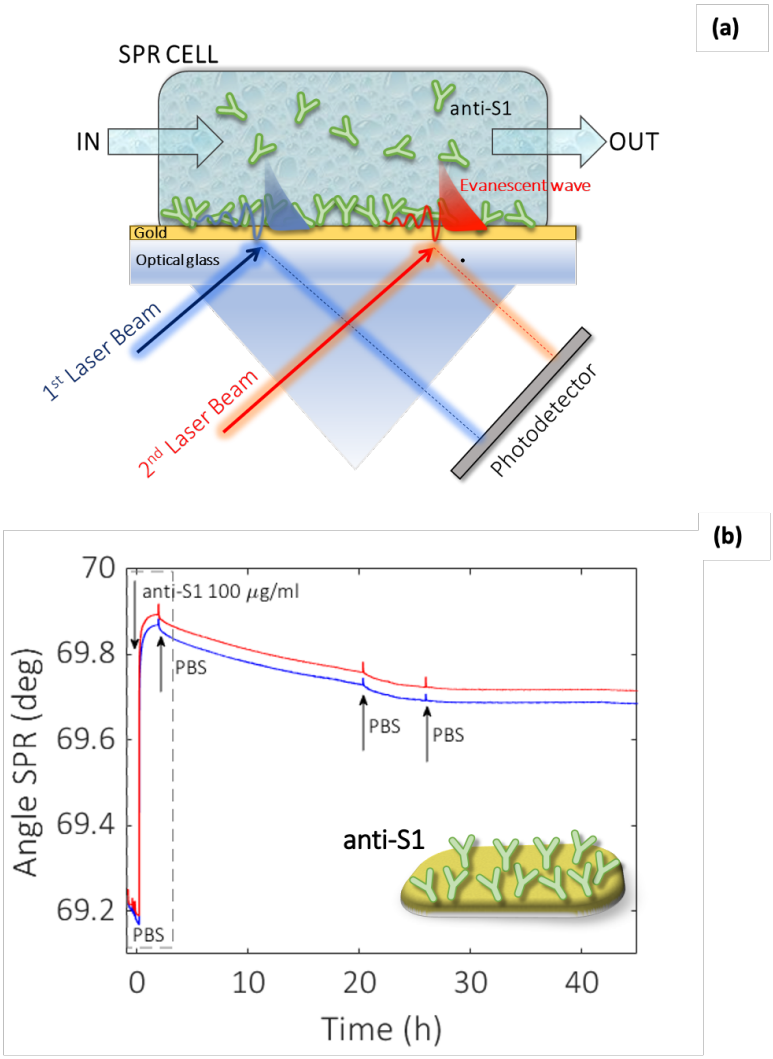

Figure S1. SPR monitoring of the anti-S1 deposition - (a) *Schematic of the Multi-Parameter SPR (MP-SPR) Navi 200-L apparatus in the Kretschmann configuration.* ***(b)*** *SPR trace (plasmon peak angle vs. time) of the physisorption of anti-S1 on the SPR gold slide. The dotted panel evidences the first three hours of the physisorption of anti-S1 film on gold and the subsequent washing steps. The SPR optical signal is recorded for the following 45 hours to accomplish the real-time monitoring of the anti-S1 stability in PBS for a much longer time. Red and blue curves are relevant to two points of the slide surface simultaneously inspected. Black arrows indicate the washing steps with PBS (i_s, 163 mM, pH 7.4).*

Therefore, under these assumptions and by substitution of **Equation S2** in **Equation S1**, **Equation S3** is derived to estimate the surface coverage Γ using the experimental angular shift, being:

$$\Gamma = \Delta\theta_{SPR} \cdot 550\ [ng/cm^2] \qquad \text{(S3)}.$$

An anti-S1 surface coverage of 374 ± 16 ng·cm^{-2}, corresponding to (1.50 ± 0.06) · 10^{12} molecules · cm^{-2}, was registered 1 hour after the first PBS washing step.

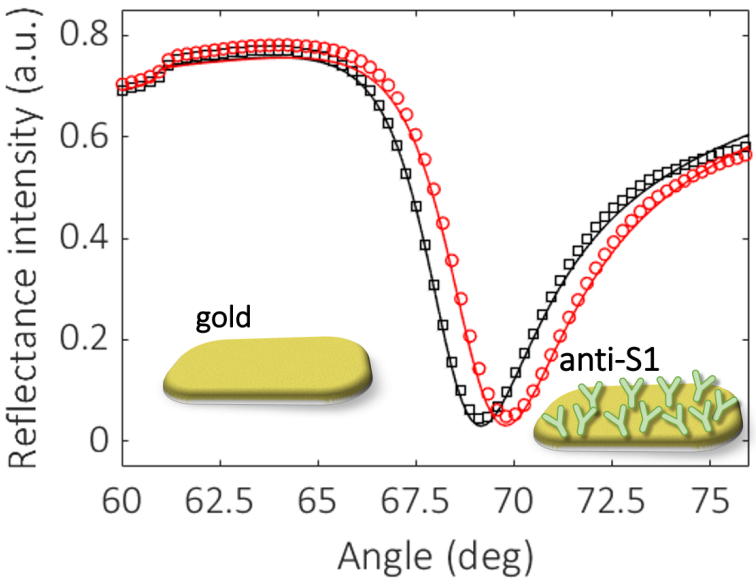

Figure S2. Comparison between SPR angular reflectivity between a bare gold and an anti-S1 covered electrode - *SPR angular reflectivity curves measured at a wavelength of 670 nm for the clean gold surface (black squares) and the physisorbed anti-S1 (red circles) in PBS; solid lines are the fitting curves (see text for details).*

The computation of the deposit thickness was based on SPR data like those measured in the first 1.5 hours in **Figure S2**. In fact, the SPR angular reflectivity curves encompassing the plasmonic peak(*51*) were fitted as shown in **Figure S2**, to achieve an accurate estimation of the thickness of the physisorbed anti-S1. These curves were simulated with a multilayer model based on the Fresnel equation using Winspall 3.02 software.(*52*) The thicknesses and apparent refractive indexes of the bare Au coated SPR slides were estimated at first, and used to simulate the thickness change upon anti-S1 physisorption. The thicknesses and optical parameters returned from the simulation of the SPR curves are summarized in **Table S1**. Those obtained for the bare Au coated slides are in perfect agreement with the nominal thicknesses declared by the SPR slides' provider and with the relevant optical parameters given in the literature.(*53*)

Table S1. *Optical parameters used for SPR data simulations. The average values along with the relative standard deviation of the simulations performed on four different sampled areas are reported.*

Layer	Thickness (nm)	Refractive Index, n	Extinction Coefficient, k
Glass BK7	0	1.52	0
Cr	1.8 ± 0.2	3.12 ± 0.05	3.6 ± 0.3
Au	48 ± 2	0.17 ± 0.03	3.79 ± 0.02
anti-S1	12 ± 1	1.38 ± 0.01	0
PBS	0	1.33	0

This clearly proves the reliability of the simulation approach used. The resulting value for the thickness of anti-S1 layer is 12 ± 1 nm, where the error bar was estimated as the relative standard deviation of the thicknesses simulated on two different replicates and four different sampled areas. To provide an estimation of the homogeneity of the biolayer thickness, the simulated SPR angular reflectivity curves were acquired from four different points on two different SPR slides. The simulated thickness of the physisorbed layer is compatible with a single monolayer of antibodies deposited on the gold slides. An immunoglobulin, such as anti-S1, holds a y-shaped structure, with typical dimensions of about 14.5 nm x 8.5 nm x 4.0 nm, with the antigen-binding sites separated by 13.7 nm.(*54*).

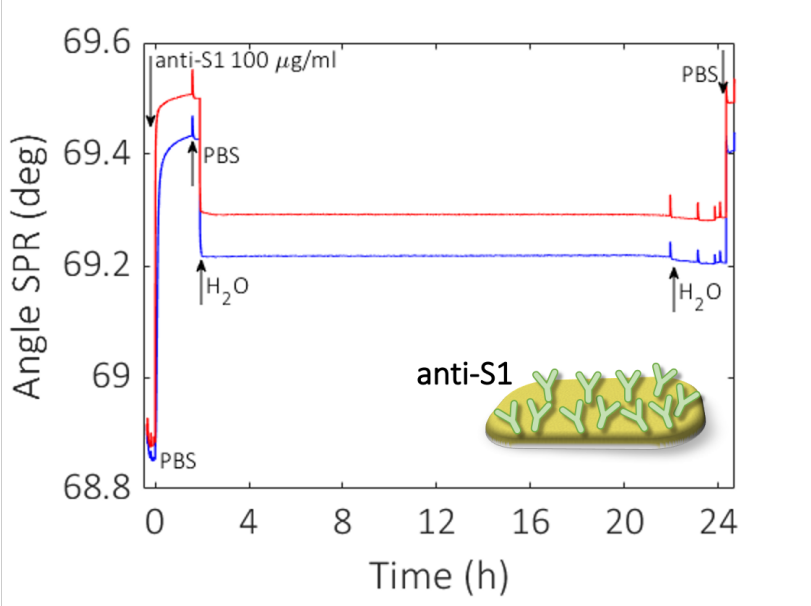

Figure S3. SPR trace of a gold slide covered by anti-S1 film deposited from PBS and kept in deionized water (HPLC grade) afterward*.- The real-time monitoring of the deposit stability in water is shown in the timeframe of 24 hours. Red and blue curves are referred to two points simultaneously tested on the same surface. Black arrows indicate the time of the injections into the SPR flow-through cell.*

To further validate the simulations, an independent estimate of the biolayer thickness is provided, by evaluating the number of anti-S1 physisorbed on the gold surface from the surface

coverage gathered from the SPR experimental data. The number of anti-S1 laying on the gold surface-exposed area (0.42 cm^2) was $(6.3 \pm 3) \cdot 10^{11}$ molecules, while the theoretical coverage of one layer of almost standing antibodies corresponds approximately to $(7 \pm 4) \cdot 10^{11}$ molecules. This implies that the anti-S1 physisorption on the gold surface led to one layer of antibodies, which is also perfectly in line with the thickness computed with the Winspall simulations.

The stability of an anti-S1 film kept in PBS or in water for several hours was also assessed. This is to prove that physisorbed proteins on gold can be very stably attached. The data about the prolonged exposure to PBS of the anti-S1 layer, are given in **Figure S1b**. After 45 hours in bare PBS of the anti-S1 film, a Γ of 280 ± 1 ng·cm^{-2}, corresponding to $(1.13 \pm 0.04) \cdot 10^{12}$ molecules·cm^{-2}, is measured. In this very prolonged exposition to PBS a 25 % overall desorption is observed. The stability of a physisorbed layer of antibodies stored in deionized water (HPLC grade) for 24 hours has been investigated too, and the corresponding SPR trace is shown in **Figure S3**. In this case, after the deposition of the anti-S1 film from a PBS solution for 1.5 hours, the surface was rinsed with PBS until a stable baseline was recorded. The SPR cell was subsequently filled with deionized water and kept in contact with the physisorbed anti-S1 layer for 24 hours. The injection of water causes an abrupt decrease in the SPR signal, which can be ascribed to a change in the refractive index of the bulk solution. A negligible decrease of the SPR signal was registered during the overnight exposure to water, showing, also in this case, extremely good stability. To quantify this figure, the refractive index of the solution in the cell was brought back to the original value, by substituting deionized water with PBS. The surface coverage measured before water injection was 326 ± 16 ng·cm^{-2}, corresponding to $(1.31 \pm 0.06) \cdot 10^{12}$ molecules·cm^{-2}. After the overnight exposure to water, the coverage was still as high as 318 ± 22 ng·cm^{-2}, corresponding to $(1.2 \pm 0.1) \cdot 10^{12}$ molecules·cm^{-2}. Remarkably, negligible anti-S1 desorption (below 3%) was registered. Thus, it is possible to infer that the anti-S1 antibodies are more prone to remain segregated onto the gold surface, instead of redissolving in deionized water.(*55*, *56*)

Section S3. Study of the SPR binding of S1 proteins to the anti-S1 physisorbed layer

The binding efficacy of the layer of physisorbed anti-S1 capturing antibodies was assessed through SPR analysis of the spike S1 target antigen binding. The biofunctionalized SPR slide was tested against the binding of S1 in a range of concentrations of 30 nM - 100 nM. The relevant sensogram, measured with a physisorbed anti-S1 SPR slide stored in PBS, is shown in **Figure S4a**. The assay was carried out by injecting S1 solutions in PBS at different concentrations. Each solution was let to interact with the anti-S1 layer for 40 minutes (**Figure S4a**) which was the typical timeframe to reach a stable SPR signal. Upon stabilization, the unbound S1 antigens were removed by rinsing with the PBS buffer solution.

The signal after each rinsing was compared to the initial baseline, acquired in PBS buffer solution, taken as the zero-level signal in the sensogram. Also in this case, the exposed sensing area was sampled in two different points (blue and red signal in **Figure S4a**). The capturing efficacy against the S1 antigens of a biofunctionalized SPR slide stored overnight in deionized water, was assessed as well. The relevant sensogram, given in **Figure S4b**, shows features that are like those registered for the SPR slide stored in PBS. The SPR angular shifts recorded upon exposure to three subsequent S1 standard solutions (30 nM, 50 nM, and 100 nM) are reported in **Table S2** for both the biofunctionalized SPR slides stored in PBS and in a deionized water (i_s = 5 μM) environment. The measured SPR responses are comparable within one standard deviation. Indeed, the data summarized in **Table S2** clearly show that physisorbed anti-S1 antibodies retain

their full biological functionality also when the layer is exposure to a deionized water environment. This is important because the bioelectronic sensor used is operated in deionized HPLC water. Remarkably, the SPR analysis demonstrates the long-term stability of physisorbed antibodies stored in deionized water, as well as how their capturing efficacy against the target antigen is fully retained under these conditions.

***Table S2**. SPR angular shift ($\Delta\theta_{SPR}$) measured for the binding of S1 protein to physisorbed anti-S1, after overnight storage of the anti-S1 biofunctionalized SPR slide in PBS and water (HPLC grade).*

Nominal Concentration S1 (nM)	PBS storage	Water storage
30	0.15 ± 0.02	0.12 ± 0.02
50	0.29 ± 0.02	0.25 ± 0.02
100	0.37 ± 0.02	0.34 ± 0.01

Last but not least, the functionalized gate was also still functional after storage for two weeks in PBS. The data are given in **Figure S5,** where the biofunctionalized SPR sensor slide was tested against the binding of S1 in the 30 nM to 100 nM concentration range.

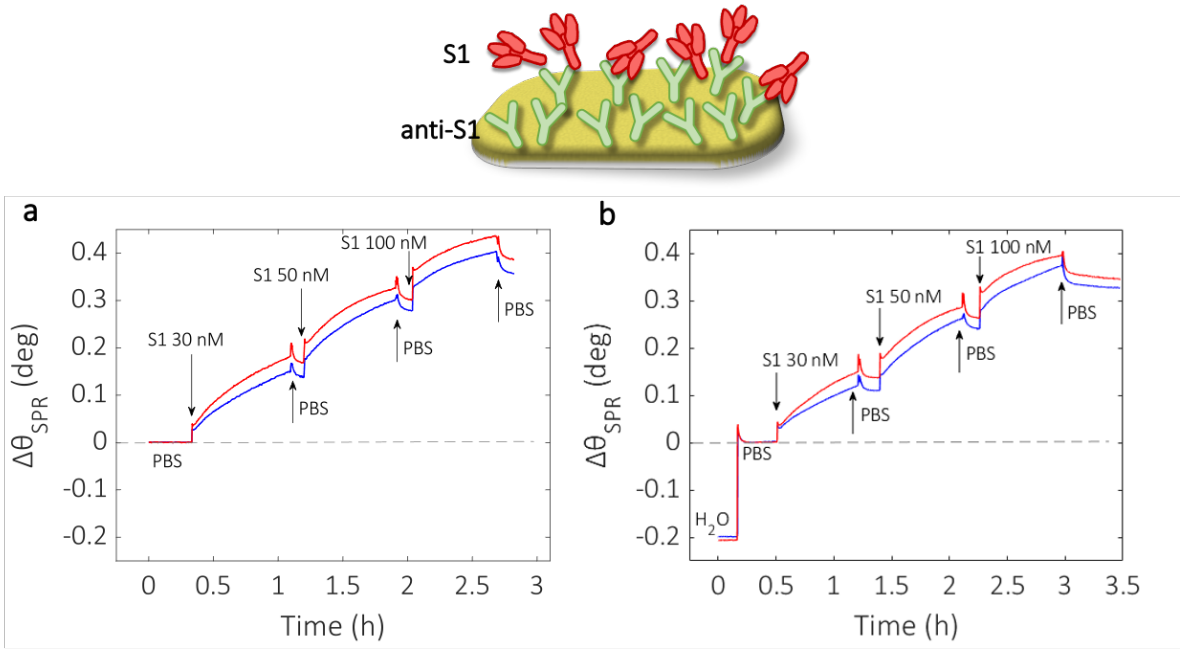

***Figure S4. S1 sensing with anti-S1 functionalized gates - (a)** Sensogram of the SPR gold slide with the anti-S1 physisorbed film exposed to different concentrations of the S1 affinity antigen. **(b)** Sensogram of the binding of the S1 antigens at the anti-S1 film on Au, kept overnight in water. Both the experiments were performed with S1 solutions whose range of concentrations is 30 nM - 100 nM.*

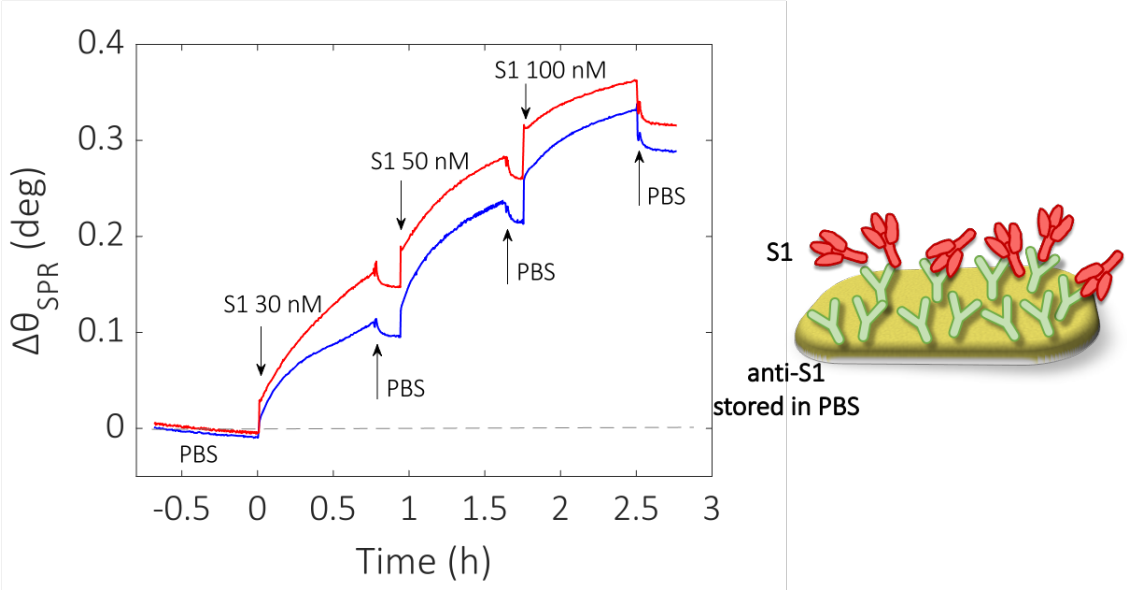

Figure S5. S1 sensing after storage of the anti-S1 functionalized gate in PBS for two weeks - *Sensogram of the SPR gold slide covered with the anti-S1 physisorbed film exposed to different concentrations of the S1 affinity antigen after storage for two weeks in PBS. The experiment was performed with S1 solutions in the 30 nM - 100 nM concentrations range.*

The sensogram of **Figure S5** shows features that are like those registered for the SPR slide freshly measured and given in **Figure S4**. The measured SPR responses are comparable within one standard deviation. These data clearly show that the physisorbed anti-S1 capturing antibodies layer retains its full biological functionality also when it is stored for two weeks in PBS.

Section S4. Assessment of the zero response at the reference electrode during sensing

The bioelectronic sensor disposable cartridge, described in the main text, encompasses a reference electrode that must return a zero-level signal throughout the whole sensing measurement. Namely, no long-lasting spurious physisorption or interaction of a substance present in the fluid to be analyzed should occur at the reference electrode. To serve on this task, the reference electrode must provide a stable level of response, or equivalently, no variations should be measured when it is exposed to different concentrations of S1. This is demonstrated by the SPR characterization of a gold electrode biofunctionalized with anti-S1 and the same gold slide coated with an antifouling proprietary conducting layer. The anti-S1 functionalized slide was prepared as described in the Methods section and was mounted in the SPR cell. The antifouling layer covering the gold surface was exposed to an increasing concentration of the target antigen S1 with concentrations ranging from 1 nM to 1 µM (**Figure S6a,** black hollow circles). The same concentration range was assayed with the SPR gold slide coated with the anti-S1 layer (**Figure S6a**, red hollow triangles). As it is apparent, the SPR angular shift measured with the antifouling polymer is negligible. Consequently, the suitability of the antifouling proprietary polymer coating for the reference electrode has been successfully demonstrated, minimizing the undesirable non-specific binding and enabling reliable detection of analytes with the *BioScreen* platform.

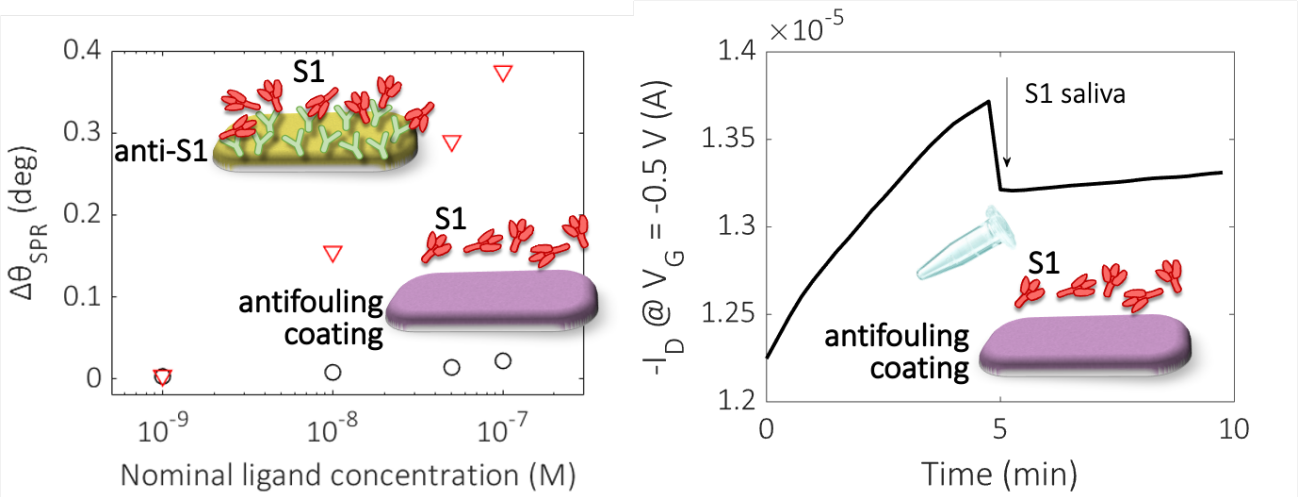

Figure S6. Antifouling properties of the reference gate - (a) *SPR angle shift as a function of the nominal ligand concentrations of di S1 analyte exposed to an anti-S1 functionalized gold slide (red-hollow-triangles) as well as with an antifouling coated gold slide (black-hollow-circles).* ***(b)*** *Transient traces of the I_D current measured at V_G = - 0.5 and V_D = - 0.1V, for a reference gate coated with an antifouling layer. The first 5 minutes are relevant to cycles 1st to 30th, measured in DI water after incubation in PIPES reference fluid; in the subsequent 5 minutes (cycles 31st-60th), the same reference gate is measured in DI water, after incubation in the sample in the whole saliva.*

The stability of the reference electrode coated with an antifouling layer immersed in whole saliva has been assessed with the *BioScreen platform* as well. **Figure S6b** shows the transient traces of the I_D current measured at V_G = - 0.5 V and V_D = - 0.1 V, for the reference gate. The first 5 minutes are relevant to cycles 1st to 30th, measured in DI water after incubation in PIPES refence fluid; in the subsequent 5 minutes (cycles 31st-60th), the same reference gate is measured in DI water, after incubation in the sample in whole saliva. The comparison with the traces measured for the negative samples shown *e.g.,* in **Figure 4b**, as well as the artificial intelligence-based analysis (*vide infra*), show that a negative response is registered with the antifouling polymer exposed to a whole saliva sample, in agreement with the SPR characterization.

Section S5. Negligible faradaic currents involved during the electronic sensing

The I_D – V_G transfer curves at a fixed V_D = - 0.1 V are shown in **Figure S7a**. The curves were measured in the forward and reverse mode to evidence the occurrence of any hysteresis. The black curve is the current measured on a sensing-extended gate biofunctionalized with anti-IgG during the 30th cycle, carried out by sweeping the gate bias from 0.2 V to - 0.5 V with steps of 10 mV in water. The blue curve is the current measured on the very same sensing gate, upon exposure to a PBS standard solution of IgM at a concentration of 6 nM, serving as a negative control experiment. The red curve has been subsequently registered on the same sensing gate, upon exposure to a PBS standard solution of IgG at a concentration of 6 fM.

The curves given in **Figure S7b** are the correspondent gate leakage currents I_G, which are always about three orders of magnitude lower than I_D. No faradaic activity can be evidenced by the I_G curve of the anti-IgG gate, proving that mild electrochemical processes have been prevented by the fine-tuning of the inspected gate voltage window. Moreover, **Figure S7b** shows also no correlation between the I_G current and the ligand concentration. These are compelling evidence, proving that the field-effect induced current I_D provides a capacity-coupled related sensing response. No other current flowing in the device can provide the same information. All

this rules out that any detrimental faradaic current is flowing through the gate and the polarizing counter electrode (**Figure 1g**), as expected in a stably operated bioelectronic transistor.(*45*)

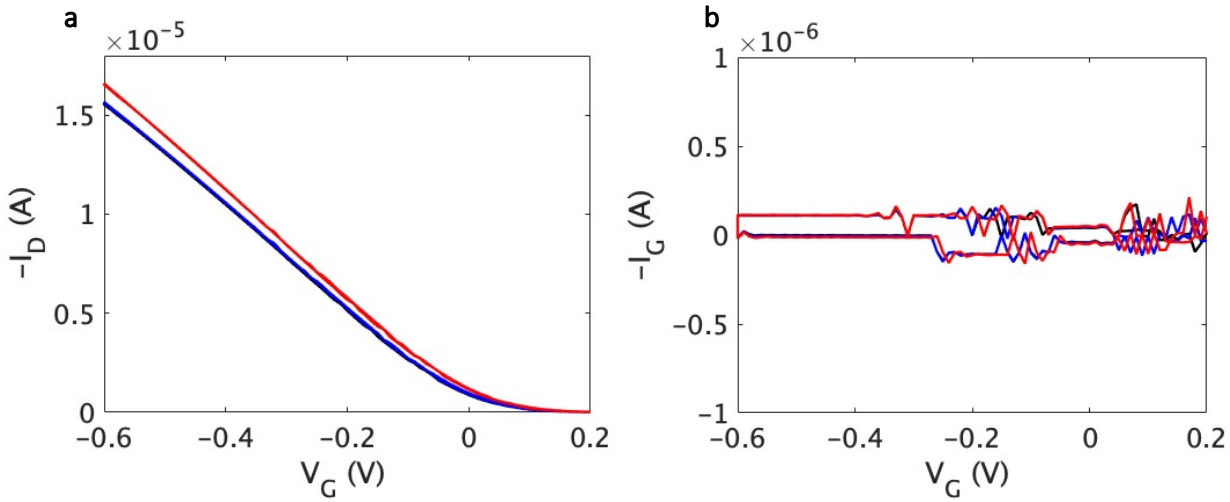

Figure S7. Limited hysteresis and leakage current during the transfer characteristics measurement - (a) *Transfer characteristics, I_D (drain current) - V_G (gate bias) at V_D (drain bias) = - 0.1 V,* ***(b)*** *along with the I_G (gate current) - V_G curve at V_D = - 0.1 V, registered upon exposure to PBS, being the baseline (black curve), PBS standard solution of IgM at a concentration of 6 nM, being the negative control experiment (blue curve) and PBS standard solution of IgG at a concentration of 6 fM, being the sensing experiment (red curve) assessed with an anti-IgG biofunctionalized sensing-extended-gate transistor (sensing-EGT). The gate is incubated in the samples to be assayed for 5 minutes. Here 30 transfer characteristics are measured; this is addressed as the cycling step, taking 5 minutes. In the panel, only the curves measured during the last (30th) cycle at each concentration assayed are shown.*

Section S6. Estimated viral concentration in real samples

The viral concentration in real samples was estimated from the S1 antigen level determined quantitatively using the LUMIPULSE SARS-CoV-2 antigen test (Fujirebio, Inc., Tokyo, Japan) in accordance with manufacturer's instructions. Saliva samples have been diluted 1:2 in Piperazine-N,N′-bis(2-ethanesulfonic acid), Piperazine-1,4-bis(2-ethanesulfonic acid), 1,4-Piperazinediethanesulfonic acid (PIPES) diluent, vortexed, transferred into a sterile tube, and centrifuged at 1000xg for 15 min. Aliquots (100 µL) of the supernatant were used for testing on the LUMIPULSE G1200 system (Fujirebio). According to the LUMIPUSE standards, samples with an antigen level > 10 pg/mL were considered positive, samples with an antigen level > 1.0 pg/mL and < 10.0 pg/mL were considered inconclusive, and samples with an antigen level < 1.0 pg/mL were considered negative. The S1 antigen level is correlated to the viral load determined by quantitative rtRT-PCR,(*57*, *58*) as follows: mean viral load ($\log_{10}$ virus/µL) of 5.4 in RT-PCR-positive samples corresponds to a mean antigen level of 4.4 $\log_{10}$ pg/mL.(*58*),(*57*) Hence, a viral concentration of 1 virus/µL (100 $\pm$ 10 viruses per 100 µl) can be estimated with a S1 antigen concentration of 0.15 pg/mL (2 10^{-15} M, 2 fM, 1.2 · 10^5 antigens in 100 µl). The supernatants collected from patients' saliva and analyzed with LUMIPULSE G1200 system have been assayed with the *BioScreen* platform. In particular, the saliva samples at different virion concentrations ranging from 1.66 virus/µL to 169.39 virus/ml were prepared by a serial dilution process in the PIPES saliva diluent from a saliva sample of a positive patient with an antigen

level of 25 pg/mL (327 fM, $2 \cdot 10^7$ in 100 µl). The nominal number of S1 antigens (# S1) at each concentration is given by the following equation: $\#S1 = cVN_A$ where c is the ligand concentration (in molarity), V is the volume of the solution in which the gate is incubated (100 µL) and N_A is the Avogadro number. The uncertainty associated with the sampling in the serial dilution can be estimated, according to Poisson's distribution, as the square root of the expected number of S1 antigens corresponding to one standard deviation.

Section S7. Evaluation of the Limit-of-Detection (LOD) and Limit-of-Identification (LOI)

A qualitative test measures the smallest amount of an analyte (*e.g.,* the targeted marker) that can be distinguished from the noise level (random error) at an acceptable level of confidence: false-positives are lower than 1% but false-negatives can reach up to 50%. This is addressed as limit-of-detection, LOD that is evaluated as the *noise-average-level (n) + 3 times the noise-standard-deviation* ($3 \cdot \sigma$).(*3*) The Gaussian distribution of the noise's statistical parameters, has been evaluated in negative control experiments. The overlap between the LOD and the gaussian distribution of the noise's statistical parameters sets the false-positive as and false-negative probabilities. Point-of-care, single-use, lateral-flow, rapid screening tests are typically qualitative and work at the LOD. While time-to-results of tens of minutes can be realistically obtained and the assay is low-cost, drawbacks include large errors (false negatives up to 50%) and LODs, in the micromolar (µM) range, often too high to effectively serve in early diagnosis.(*59*),(*60*) The *BioScreen* platform is proven capable of reliably discriminating a sample containing not even one virus from those with at least one. Reliability is guaranteed by operating at the *limit-of-identification*, evaluated as the *noise-average-level (n) + 6 times the noise-standard-deviation* ($LOI = n + 6 \cdot \sigma$) that assures a level of confidence larger than 99 % and, differently from the LOD, both false positives and false negatives, are lower than 1%.

Section S8. The *BioScreen* Artificial Intelligence (AI) based binary classifier

In **Figure S8** the transient exemplary traces of the I_D current measured at V_G = - 0.5V and V_D = - 0.1V, for a positive (**panel-a**, red curves) and a negative (**panel-b**, blue curves) sample, are shown. The cycles from 1st to 30th (first 5 minutes) are measured after incubating the sensing-gate in the reference fluid for 5 minutes. The cycles from 31st to 60th (subsequent 5 minutes) are measured after incubating the same gate in the sample to be assayed for 5 minutes. These sets of measurements addressed as the cycling of the gate electrode (see Method section), are carried out in DI water to minimize the screening of the electrostatic effects, by maximizing the Debye length. The curves in **Figure S8** are relevant to the immunometric system involving an anti-SARS-CoV-2 Spike-S1 (anti-S1) functionalized gate exposed to the non-binding MERS-CoV-2 Spike-S1 for the negative sample, and to the SARS-CoV-2 Spike-S1 (S1) for the positive one. The two assays are carried out in the PBS reference fluid and in whole blood. Relevantly, the evolution of the current with time evidences a characteristic dynamic behavior.

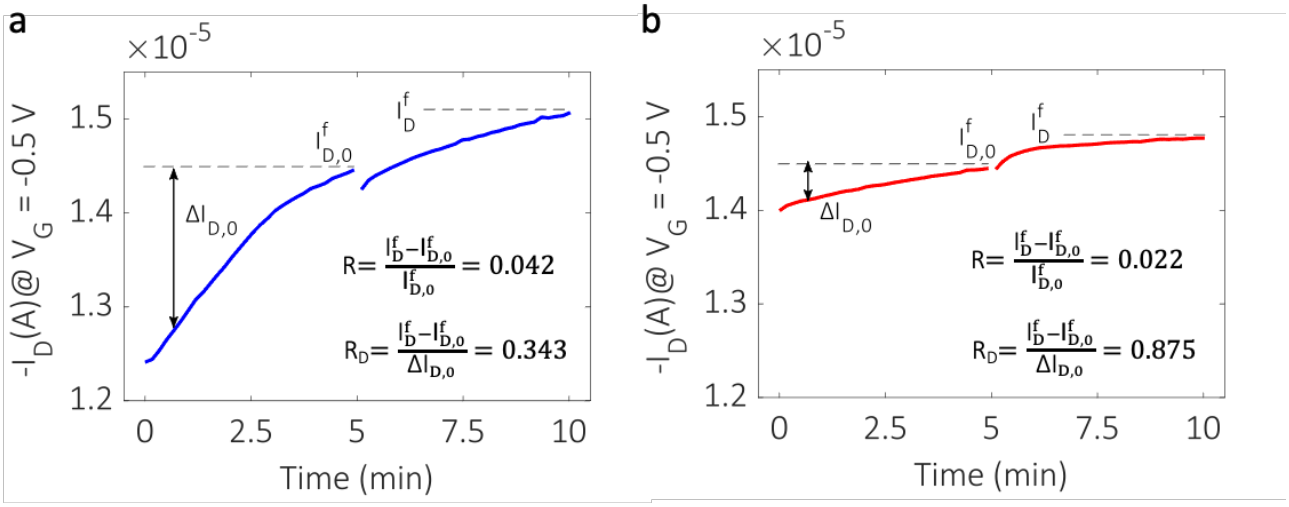

Figure S8. Examples of sensing measurements with the Bioscreen system - *Two examples of transient traces of the I_D current measured at V_G = -0.5 and V_D = -0.1V, for a negative (**panel-a**, blue curves) and a positive sample (**panel-b**, red curves). The cycles from 1st to 30th are carried out in DI water after incubating the sensing gate in the reference fluid. The cycles from 31st to 60th are measured in DI water after incubating the same gate in the sample to be assayed. In **panel-a**, the trace is relevant to the response of a gate functionalized with anti-S1 measured in PBS (reference fluid) that is then measured in whole blood added with the non-binding MERS-CoV-2 Spike-S1. As the latter does not bind to anti-S1, this is a negative sample. In **panel-b** a second gate functionalized with the anti-S1 is first measured in PBS and afterward, the anti-S1 assays S1 added in whole blood. This is a positive sample.*

Typically, a sensing response is taken as the current fractional change with respect to the baseline level.(*39*) In the present case, given the dynamic behavior of the gate, the last point of each set of 30th cycles is considered and the sensing response is defined by:

$$R = \frac{(I_D^f - I_{D,0}^f)}{I_{D,0}^f} \qquad \text{(S4)}$$

where I_D^f is the *final* drain current value (at V_G = - 0.5 V and V_D = - 0.1 V) measured after incubation of the gate in the sample, at the end of the 60th cycle while $I_{D,0}^f$ is the *final* current value (measured at V_G = -0.5 V and V_D = -0.1 V), in the reference fluid (baseline), at the end of the 30th cycle. As it is apparent the value for the R response (called "*feature*" in the artificial intelligent algorithm, *vide infra*) for the negative sample (**Figure S8, a-panel**) is + 0.042 while it goes down to + 0.022 in the positive sample (**Figure S8, b-panel**). The choice of the R parameter in this exemplary case, can lead to an erroneous classification so **panel-a** can feature a false-positive while **panel-b** can feature a false-negative, depending on the chosen threshold.

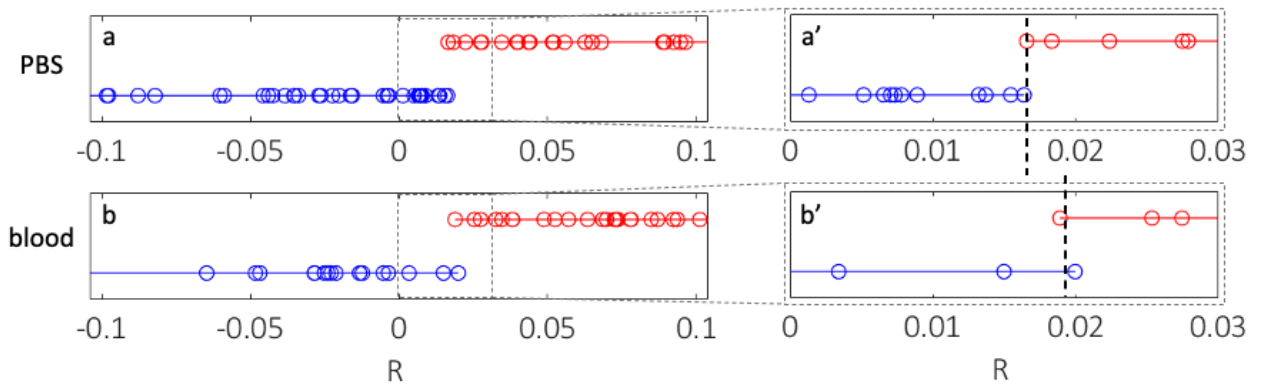

Figure S9. R feature output of the BioScreen responses in PBS and blood - *In **panel-a** R values from the assays carried out in PBS (42 assays) are shown while **panel-b** shows R values for the data gathered in whole blood (40 assays). **Panel-a'** and **panel-b'** are zooms into the central area highlighted with the black dotted lines. In all panels, blue dots feature the negative samples while the red ones indicate the positive samples. The vertical black dotted lines in **panel-a'** and **panel-b'** mark the central confusion region where the positive and the negative outputs overlap, resulting in 2% of false positives and 11% false negatives.*

Figure S9 shows the R values computed for all the assays carried out in PBS (**panel-a**) and in whole blood (**panel-b**). Here the outputs relevant to different immunoassays (details in Method section) are included. Negative samples are given as blue dots while the positive ones are given as red dots and the R values range from - 0.10 to + 0.10. **Panel-a'** and **panel-b'** are the zooms into the central regions and the vertical black dotted lines mark where the positive and the negative samples overlap. This is around 0.017 for the data in PBS and around 0.020 for those in whole blood. These overlaps define *confusion regions* where false-positive and false-negative errors occur as in the exemplary cases shown in **Figure S8** that leads to a misclassification whatever threshold is selected. As it is apparent, by using only the *R-feature* to perform the binary classification of our sample, leads to a rather large number of points falling in the *confusion region*. More quantitatively, applying only *feature* R to classify the whole database of 240 samples, results in a 2% of false-positives and 11% false-negatives. This results into a *diagnostic sensitivity* = true-positives/(true-positives + false-negatives) = 89.9 %, a *diagnostic specificity* = true-negatives/(true-negatives + false-positives) = 97.8 % and a *diagnostic accuracy* = (true-positives + true-negatives)/(true-negatives + false-positives + false-negatives + true-positives) = 93.5 %. Such a high error rate would not make the *BioScreen* platform significantly better than already commercially available point-of-care systems (see **Table S3** in **Section S9**). Moreover, the approach lacks generality as the degree of overlap depends on the fluid (PBS, blood, saliva, …) in which the assay is carried out (data not shown).

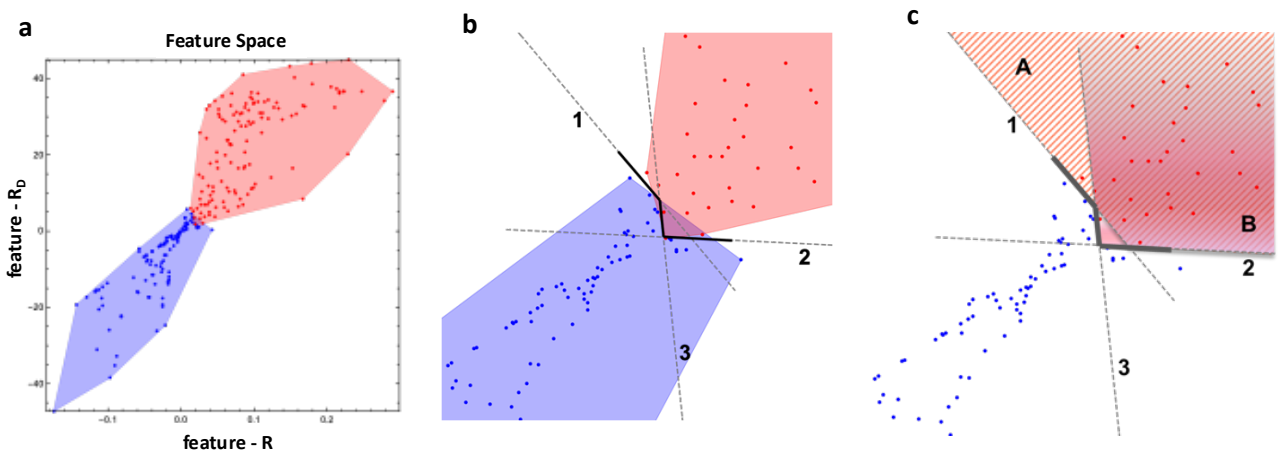

Figure S10. 2D Feature Space for the R and R_D values - (a) *All the 240 samples assayed in the present study plotted in the 2D Feature Space. The negative samples are given in blue while the positive ones are given in red.* ***(b)*** *Zoom into the central region of the plot; black lines 1, 2, and 3 are the boundaries defined by the first layer perceptrons of the binary classifier (see text for details).* ***(c)*** *The convex regions A and B are defined by the perceptrons in the second (hidden) layer of the binary classifier (see text for details).*

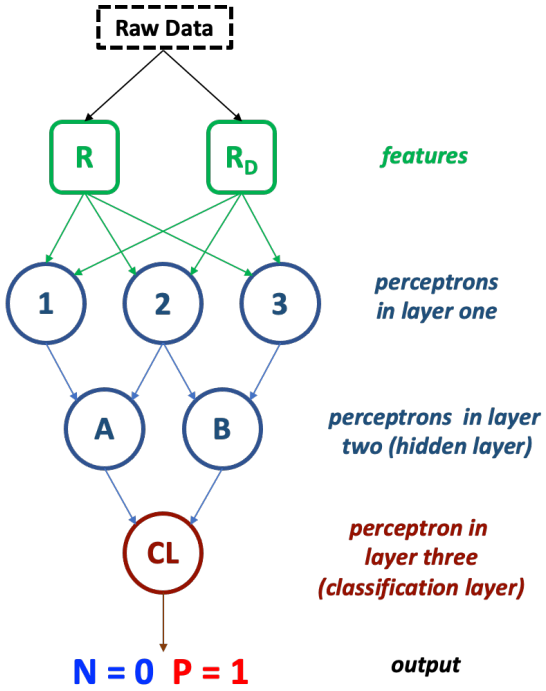

Figure S11. Multi-Layer Perceptron network, MLPn, binary classifier *- reading raw sensor data is based on two features, six perceptrons, and three layers. It produces the binary output from the classification layer node CL setting 0 for negative answers and 1 for positive ones.*

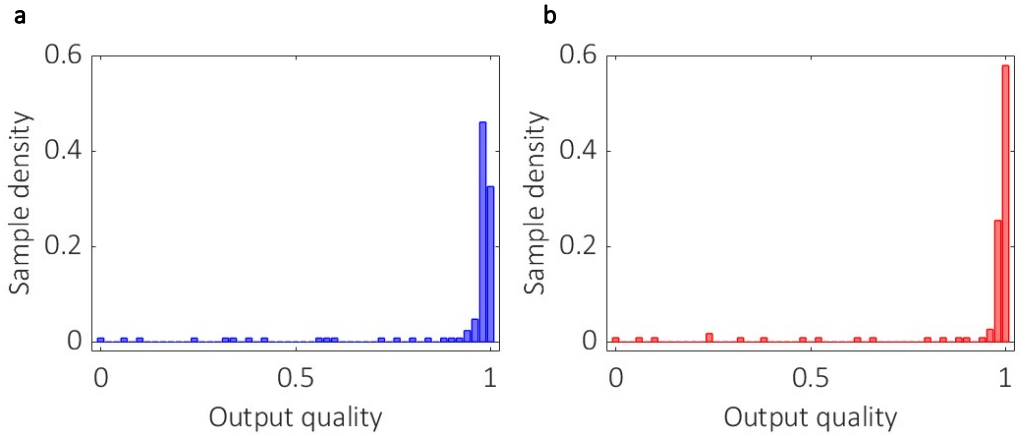

Figure S12. BioScreen output quality parameter *- Histograms of the density of* ***(a)*** *negative and* ***(b)*** *positive samples vs. the BioScreen output quality parameter for all the 240 samples assayed. Blue bars stand for negative outputs while red ones address positive answers.*

Section S9. Benchmarking BioScreen data

The benchmark of the *BioScreen* platform against the most advanced sensor technologies and platforms is displayed in **Table 3S**. The most relevant figures-of-merit, including time-to-results, output signal, LOD, LOI, diagnostic sensitivity, specificity, selectivity, AUC (Area Under the Curve in a Receiver Operator Characteristic graph), demonstration of POC, biofunctionalization time, and the shelf-life of the gate already covered with the capturing layer. This is relevant information to provide because the biofunctionalization process can be time-consuming and, if it has to be carried out just before the sensing, a much longer time-to-results is needed. The best performance level for each figure of merit is evidenced, highlighting the entry in bold.

Table S3: *Benchmarking the BioScreen platform. The comparison accounts for the state-of-art where real-sample analysis is demonstrated.*

Technology	Output	LOD (#/100µL)	LOI (#/100mL)	Time to results (min.)	Label free	Diagnostic Sensitivity	Diagnostic Specificity	Diagnostic Accuracy	AUC	POC	Biofunc. time (h)	Shelf life (weeks)	Year
1. Electrolyte-gated organic FET	Electrical	**1**	N.A.	30	**Yes**	N.A.	N.A.	N.A.	N.A.	No	16	N.A.	2018
2. Graphene FET	Electrical	**N.A.**	N.A.	**1**	**Yes**	N.A.	N.A.	N.A.	N.A.	No	5	N.A.	2020
3. Nanobody OECT	Electrical	**1**	N.A.	**15**	**Yes**	N.A.	N.A.	N.A.	N.A.	No	3	1	2021
4. Immunochromatographic	Visual	10^8	N.A.	**15**	No	57,7%	**99,5%**	82,6%	N.A.	**Yes**	N.A.	N.A.	2020
5. Electrochemical	**Digital**	10^8	N.A.	60	No	**100%**	**100%**	N.A.	**0,998**	**Yes**	**2**	N.A.	2021
6. Electrochemical magnetic bead	Electrical	10^9	N.A.	40	No	68%	**100%**	72%	N.A.	No	**2**	N.A.	2020
7. DETECTR	Visual	10^3	N.A.	45	No	95%	**100%**	N.A.	N.A.	No	N.A.	N.A.	2020
8. Colorimetric RT-LAMP	Visual	**1**	N.A.	45	**Yes**	N.A.	**99,7%**	N.A.	N.A.	**Yes**	N.A.	N.A.	2020
9. ID now platform - Abbott	**Digital**	12.5	N.A.	**13**	No	90%	N.A.	N.A.	N.A.	**Yes**	N.A.	**12**	2020
10. *BioScreen* platform	**Digital**	**1**	**1**	**21,2**	**Yes**	**99,2%**	**99,2%**	**99,2%**	**1,000**	**Yes**	**2**	**3**	this work

entry: 1 ,(*39*) 2,(*16*) 3,(*26*) 4,(*11*) 5,(*12*) 6,(*44*) 7,(*13*) 8,(*7*) 9(*8*)

The entries in **Table 3S** show how the *BioScreen* platform uniquely reaches best performance levels, compared to the state-of-the-art platforms and technologies, in all the categories.

Movie S1.

Caption to the movie S1: The whole BioScreen assay procedure comprising all the needed steps that are completed in 21 minutes

REFERENCES AND NOTES

1. World Health Organization, *The Top 10 Causes of Death—Factsheet* (World Health Organization, 2020), pp. 1–9.

2. O. Vandenberg, D. Martiny, O. Rochas, A. van Belkum, Z. Kozlakidis, Considerations for diagnostic COVID-19 tests. *Nat. Rev. Microbiol.* **19**, 171–183 (2021).

3. M. Thompson, S. L. R. Ellison, R. Wood, Harmonized guidelines for single-laboratory validation of methods of analysis (IUPAC Technical Report). *Pure Appl. Chem.* **74**, 835–855 (2002).

4. H. R. Boehringer, B. J. O'Farrell, Lateral flow assays in infectious disease diagnosis. *Clin. Chem.* **68**, 52–58 (2021).

5. R. Arnaout, R. A. Lee, G. R. Lee, C. Callahan, A. Cheng, C. F. Yen, K. P. Smith, R. Arora, J. E. Kirby, The limit of detection matters: The case for benchmarking severe acute respiratory syndrome coronavirus 2 testing. *Clin. Infect. Dis.* **73,** e3042–e3046 (2021).

6. K. J. Land, D. I. Boeras, X. S. Chen, A. R. Ramsay, R. W. Peeling, REASSURED diagnostics to inform disease control strategies, strengthen health systems and improve patient outcomes. *Nat. Microbiol.* **4**, 46–54 (2019).

7. V. L. Dao Thi, K. Herbst, K. Boerner, M. Meurer, L. P. M. Kremer, D. Kirrmaier, A. Freistaedter, D. Papagiannidis, C. Galmozzi, M. L. Stanifer, S. Boulant, S. Klein, P. Chlanda, D. Khalid, I. B. Miranda, P. Schnitzler, H. G. Kräusslich, M. Knop, S. Anders, A colorimetric RT-LAMP assay and LAMP-sequencing for detecting SARS-CoV-2 RNA in clinical samples. *Sci. Transl. Med.* **12**, eabc7075 (2020).

8. Abbot ID NOW, www.abbott.com/IDNOW.html?CID=OUS_OK.

9. B. Ning, T. Yu, S. Zhang, Z. Huang, D. Tian, Z. Lin, A. Niu, N. Golden, K. Hensley, B. Threeton, C. J. Lyon, X. M. Yin, C. J. Roy, N. S. Saba, J. Rappaport, Q. Wei, T. Y. Hu, A smartphone-read ultrasensitive and quantitative saliva test for COVID-19. *Sci. Adv.* **7**, eabe3703 (2021).

10. N. Panpradist, E. C. Kline, R. G. Atkinson, M. Roller, Q. Wang, I. T. Hull, J. H. Kotnik, A. K. Oreskovic, C. Bennett, D. Leon, V. Lyon, S. D. Gilligan-Steinberg, P. D. Han, P. K. Drain, L. M. Starita, M. J. Thompson, B. R. Lutz, Harmony COVID-19: A ready-to-use kit, low-cost detector, and smartphone app for point-of-care SARS-CoV-2 RNA detection. *Sci. Adv.* **7**, eabj1281 (2021).

11. P. Mertens, N. De Vos, D. Martiny, C. Jassoy, A. Mirazimi, L. Cuypers, S. Van den Wijngaert, V. Monteil, P. Melin, K. Stoffels, N. Yin, D. Mileto, S. Delaunoy, H. Magein, K. Lagrou, J. Bouzet, G. Serrano, M. Wautier, T. Leclipteux, M. Van Ranst, O. Vandenberg, Development and potential usefulness of the COVID-19 Ag Respi-Strip diagnostic assay in a pandemic context. *Front. Med.* **7**, 225 (2020).

12. N. K. Singh, P. Ray, A. F. Carlin, C. Magallanes, S. C. Morgan, L. C. Laurent, E. S. Aronoff-Spencer, D. A. Hall, Hitting the diagnostic sweet spot: Point-of-care SARS-CoV-2 salivary antigen testing with an off-the-shelf glucometer. *Biosens. Bioelectron.* **180**, 113111 (2021).

13. J. P. Broughton, X. Deng, G. Yu, C. L. Fasching, V. Servellita, J. Singh, X. Miao, J. A. Streithorst, A. Granados, A. Sotomayor-gonzalez, K. Zorn, A. Gopez, E. Hsu, W. Gu, S. Miller, C. Pan, H. Guevara, D. A. Wadford, J. S. Chen, C. Y. Chiu, CRISPR – Cas12-based detection of SARS-CoV-2. *Nat. Biotechnol.* **38**, 870–874 (2020).

14. V. Parkula, M. Berto, C. Diacci, B. Patrahau, M. Di Lauro, A. Kovtun, A. Liscio, M. Sensi, P. Samorì, P. Greco, C. A. Bortolotti, F. Biscarini, Harnessing selectivity and sensitivity in electronic biosensing: A novel lab-on-chip multigate organic transistor. *Anal. Chem.* **92**, 9330–9337 (2020).

15. D. Rani, Y. Singh, M. Salker, X. T. Vu, S. Ingebrandt, V. Pachauri, Point-of-care-ready nanoscale ISFET arrays for sub-picomolar detection of cytokines in cell cultures. *Anal. Bioanal. Chem.* **412**, 6777–6788 (2020).

16. G. Seo, G. Lee, M. J. Kim, S. H. Baek, M. Choi, K. B. Ku, C. S. Lee, S. Jun, D. Park, H. G. Kim, S. J. Kim, J. O. Lee, B. T. Kim, E. C. Park, S. Il Kim, Rapid detection of COVID-19 causative virus (SARS-CoV-2) in human nasopharyngeal swab specimens using field-effect transistor-based biosensor. *ACS Nano* **14**, 5135–5142 (2020).

17. Q. Liu, C. Zhao, M. Chen, Y. Liu, Z. Zhao, F. Wu, Z. Li, P. S. Weiss, A. M. Andrews, C. Zhou, Flexible multiplexed In_2O_3 nanoribbon aptamer-field-effect transistors for biosensing. *iScience* **23**, 101469 (2020).

18. J. W. Ko, J. M. Woo, A. Jinhong, J. H. Cheon, J. H. Lim, S. H. Kim, H. Chun, E. Kim, Y. J. Park, Multi-order dynamic range DNA sensor using a gold decorated SWCNT random network. *ACS Nano* **5**, 4365–4372 (2011).

19. Y. Liang, M. Xiao, D. Wu, Y. Lin, L. Liu, J. He, G. Zhang, L. M. Peng, Z. Zhang, Wafer-scale uniform carbon nanotube transistors for ultrasensitive and label-free detection of disease biomarkers. *ACS Nano* **14**, 8866–8874 (2020).

20. R. Hajian, S. Balderston, T. Tran, T. deBoer, J. Etienne, M. Sandhu, N. A. Wauford, J. Y. Chung, J. Nokes, M. Athaiya, J. Paredes, R. Peytavi, B. Goldsmith, N. Murthy, I. M. Conboy, K. Aran, Detection of unamplified target genes via CRISPR–Cas9 immobilized on a graphene field-effect transistor. *Nat. Biomed. Eng.* **3**, 427–437 (2019).

21. E. MacChia, F. Torricelli, P. Bollella, L. Sarcina, A. Tricase, C. Di Franco, R. Österbacka, Z. M. Kovács-Vajna, G. Scamarcio, L. Torsi, Large-area interfaces for single-molecule label-free bioelectronic detection. *Chem. Rev.* **122**, 4636–4699 (2022).

22. E. Macchia, P. Romele, K. Manoli, M. Ghittorelli, M. Magliulo, Z. M. Kovács-Vajna, F. Torricelli, L. Torsi, Ultra-sensitive protein detection with organic electrochemical transistors printed on plastic substrates. *Flex. Print. Electron.* **3**, 034002 (2018).

23. X. Wang, Y. Wang, Y. Wu, Y. Xiao, A highly sensitive and versatile chiral sensor based on a top-gate organic field effect transistor functionalized with thiolated β-cyclodextrin. *Analyst* **144**, 2611–2617 (2019).

24. Y. Wu, X. Wang, X. Li, Y. Xiao, Y. Wang, Cyclodextrin derivatives functionalized highly sensitive chiral sensor based on organic field-effect transistor. *Chin. Chem. Lett.* **31**, 99–102 (2019).

25. S. K. Sailapu, E. Macchia, I. Merino-Jimenez, J. P. Esquivel, L. Sarcina, G. Scamarcio, S. D. Minteer, L. Torsi, N. Sabaté, Standalone operation of an EGOFET for ultra-sensitive detection of HIV. *Biosens. Bioelectron.* **156**, 112103 (2020).

26. K. Guo, S. Wustoni, A. Koklu, E. Díaz-Galicia, M. Moser, A. Hama, A. A. Alqahtani, A. N. Ahmad, F. S. Alhamlan, M. Shuaib, A. Pain, I. McCulloch, S. T. Arold, R. Grünberg, S. Inal, Rapid single-molecule detection of COVID-19 and MERS antigens via nanobody-functionalized organic electrochemical transistors. *Nat. Biomed. Eng.* **5**, 666–677 (2021).

27. E. Macchia, K. Manoli, B. Holzer, C. Di Franco, M. Ghittorelli, F. Torricelli, D. Alberga, G. F. Mangiatordi, G. Palazzo, G. Scamarcio, L. Torsi, Single-molecule detection with a millimetre-sized transistor. *Nat. Commun.* **9**, 3223 (2018).

28. E. Macchia, K. Manoli, C. Di Franco, R. A. Picca, R. Österbacka, G. Palazzo, F. Torricelli, G. Scamarcio, L. Torsi, Organic field-effect transistor platform for label-free, single-molecule detection of genomic biomarkers. *ACS Sens.* **5**, 1822–1830 (2020).

29. E. Macchia, A. Tiwari, K. Manoli, B. Holzer, N. Ditaranto, R. A. Picca, N. Cioffi, C. Di Franco, G. Scamarcio, G. Palazzo, L. Torsi, Label-free and selective single-molecule bioelectronic sensing with a millimeter-wide self-assembled monolayer of anti-immunoglobulins. *Chem. Mater.* **31**, 6476–6483 (2019).

30. E. Macchia, K. Manoli, B. Holzer, C. Di Franco, R. A. Picca, N. Cioffi, G. Scamarcio, G. Palazzo, L. Torsi, Selective single-molecule analytical detection of C-reactive protein in saliva with an organic transistor. *Anal. Bioanal. Chem.* **411**, 4899–4908 (2019).

31. E. Macchia, L. Sarcina, R. A. Picca, K. Manoli, C. Di Franco, G. Scamarcio, L. Torsi, Ultra-low HIV-1 p24 detection limits with a bioelectronic sensor. *Anal. Bioanal. Chem.* **412**, 811–818 (2020).

32. R. A. Picca, K. Manoli, E. Macchia, L. Sarcina, C. Di Franco, N. Cioffi, D. Blasi, R. Österbacka, F. Torricelli, G. Scamarcio, L. Torsi, Ultimately sensitive organic bioelectronic transistor sensors by materials and device structure design. *Adv. Funct. Mater.* **30**, 1904513 (2020).

33. E. Macchia, L. Sarcina, C. Driescher, Z. Gounani, A. Tewari, R. Osterbacka, G. Palazzo, A. Tricase, Z. M. Kovács-Vajna, F. Viola, F. Modena, M. Caironi, F. Torricelli, I. Esposito, L. Torsi, Single-molecule bioelectronic label-free assay of both protein and genomic markers of pancreatic mucinous cysts' in whole blood serum. *Adv. Electron. Mater.* **7**, 2100304 (2021).

34. E. Macchia, K. Manoli, C. Di Franco, G. Scamarcio, L. Torsi, New trends in single-molecule bioanalytical detection. *Anal. Bioanal. Chem.* **412**, 5005–5014 (2020).

35. C. H. Chu, I. Sarangadharan, A. Regmi, Y. W. Chen, C. P. Hsu, W. H. Chang, G. Y. Lee, J. I. Chyi, C. C. Chen, S. C. Shiesh, G. Bin Lee, Y. L. Wang, Beyond the Debye length in high ionic strength solution: Direct protein detection with field-effect transistors (FETs) in human serum. *Sci. Rep.* **7**, 5256 (2017).

36. M. Kaisti, Detection principles of biological and chemical FET sensors. *Biosens. Bioelectron.* **98**, 437–448 (2017).

37. L. Kergoat, L. Herlogsson, D. Braga, B. Piro, M. C. Pham, X. Crispin, M. Berggren, G. Horowitz, A water-gate organic field-effect transistor. *Adv. Mater.* **22**, 2565–2569 (2010).

38. F. Torricelli, D. Z. Adrahtas, F. Biscarini, A. Bonfiglio, C. A. Bortolotti, C. D. Frisbie, I. Mcculloch, E. Macchia, G. G. Malliaras, Electrolyte- gated transistors for enhanced performance bioelectronics. *Nat. Rev. Methods Primers* **1**, 66 (2021).

39. O. Elemento, C. Leslie, J. Lundin, G. Tourassi, Artificial intelligence in cancer research, diagnosis and therapy. *Nat. Rev. Cancer* **21**, 747–752 (2021).

40. A. Gupta, Anjum, S. Gupta, R. Katarya, InstaCovNet-19: A deep learning classification model for the detection of COVID-19 patients using chest x-ray. *Appl. Soft Comput.* **99**, 106859 (2021).

41. X. Liu, L. Faes, A. U. Kale, S. K. Wagner, D. J. Fu, A. Bruynseels, T. Mahendiran, G. Moraes, M. Shamdas, C. Kern, J. R. Ledsam, M. K. Schmid, K. Balaskas, E. J. Topol, L. M. Bachmann, P. A. Keane, A. K. Denniston, A comparison of deep learning performance against health-care professionals in detecting diseases from medical imaging: A systematic review and meta-analysis. *Lancet Digit. Health* **1**, e271–e297 (2019).

42. R. M. Hristev, *The ANN Book* (1998).

43. L. Fabiani, M. Saroglia, G. Galatà, R. De Santis, S. Fillo, V. Luca, G. Faggioni, N. D'Amore, E. Regalbuto, P. Salvatori, G. Terova, D. Moscone, F. Lista, F. Arduini, Magnetic beads combined with carbon black-based screen-printed electrodes for COVID-19: A reliable and miniaturized electrochemical immunosensor for SARS-CoV-2 detection in saliva. *Biosens. Bioelectron.* **171**, 112686 (2021).

44. E. Macchia, R. A. Picca, K. Manoli, C. Di Franco, D. Blasi, L. Sarcina, N. Ditaranto, N. Cioffi, R. Österbacka, G. Scamarcio, F. Torricelli, L. Torsi, About the amplification factors in organic bioelectronic sensors. *Mater. Horiz.* **7**, 999–1013 (2020).

45. E. Kretschmann, H. Raether, Notizen: Radiative decay of non radiative surface plasmons excited by light. *Z. Naturforsch. A* **23**, 2135–2136 (1968).

46. E. T. Gedig, in *Handbook of Surface Plasmon Resonance*, Richard B. M. Schasfoort, Ed. (The Royal Society of Chemistry, ed. 2, 2017), pp. 173–220.

47. J. Homola, Surface plasmon resonance sensors for detection of chemical and biological species. *Chem. Rev.* **108**, 462–493 (2008).

48. J. A. De Feijter, J. Benjamins, F. A. Veer, Ellipsometry as a tool to study the adsorption behavior of synthetic and biopolymers at the air–water interface. *Biopolymers* **17**, 1759–1772 (1978).

49. V. Ball, J. J. Ramsden, Buffer dependence of refractive index increments of protein solutions. *Biopolymers* **46**, 489–492 (1998).

50. C. M. Miyazaki, F. M. Shimizu, M. Ferreira, Surface plasmon resonance (SPR) for sensors and biosensors. *Nanocharacterization Tech.*, 183–200 (2017).

51. Winspall 3.02 software, p. 3.

52. Refractive Index reference value; https://refractiveindex.info/.

53. Y. H. Tan, M. Liu, B. Nolting, J. G. Go, J. Gervay-Hague, G. Y. Liu, A nanoengineering approach for investigation and regulation of protein immobilization. *ACS Nano* **2**, 2374–2384 (2008).

54. D. Male, J. Brostoff, D. B. Roth, I. Roitt, *Immunology* (Elsevier, ed. 8, 2013), vol. 4.

55. A. K. Abbas, A. H. Lichtman, S. Pillai, (Saunders, ed. 5, 2003), pp. 189–214.

56. Y. Hirotsu, M. Maejima, M. Shibusawa, K. Amemiya, Y. Nagakubo, K. Hosaka, H. Sueki, M. Hayakawa, H. Mochizuki, T. Tsutsui, Y. Kakizaki, Y. Miyashita, M. Omata, Prospective study of 1308 nasopharyngeal swabs from 1033 patients using the LUMIPULSE SARS-CoV-2 antigen test: Comparison with RT-qPCR. *Int. J. Infect. Dis.* **105**, 7–14 (2021).

57. Y. Hirotsu, M. Maejima, M. Shibusawa, Y. Nagakubo, K. Hosaka, K. Amemiya, H. Sueki, M. Hayakawa, H. Mochizuki, T. Tsutsui, Y. Kakizaki, Y. Miyashita, S. Yagi, S. Kojima, M. Omata, Comparison of automated SARS-CoV-2 antigen test for COVID-19 infection with quantitative RT-PCR using 313 nasopharyngeal swabs, including from seven serially followed patients. *Int. J. Infect. Dis.* **99**, 397–402 (2020).

58. E. B. Bahadır, M. K. Sezgintürk, Lateral flow assays: Principles, designs and labels. *Trends Anal. Chem.* **82**, 286–306 (2016).

59. T. Mahmoudi, M. de la Guardia, B. Shirdel, A. Mokhtarzadeh, B. Baradaran, Recent advancements in structural improvements of lateral flow assays towards point-of-care testing. *Trends Anal. Chem.* **116**, 13–30 (2019).